



Evolution of Flare Activity in GKM Stars Younger than 300 Myr over Five Years of TESS Observations

ADINA D. FEINSTEIN ^{1,*} DARRYL Z. SELIGMAN ^{2,†} KEVIN FRANCE ^{1,3,4} JONATHAN GAGNÉ ^{5,6} AND
ADAM KOWALSKI ^{3,7}

¹Laboratory for Atmospheric and Space Physics, University of Colorado Boulder, UCB 600, Boulder, CO 80309

²Department of Astronomy and Carl Sagan Institute, Cornell University, 122 Sciences Drive, Ithaca, NY 14853

³Department of Astrophysical and Planetary Sciences, University of Colorado, UCB 389, Boulder, CO 80309, USA

⁴Center for Astrophysics and Space Astronomy, University of Colorado, 389 UCB, Boulder, CO 80309, USA

⁵Planétarium Rio Tinto Alcan, Escape pour la Vie, 4801 av. Pierre-de Coubertin, Montréal, Québec, Canada

⁶Institute for Research on Exoplanets, Université de Montréal, Département de Physique, C.P. 6128 Succ. Centre-ville, Montréal, QC H3C 3J7, Canada

⁷National Solar Observatory, University of Colorado Boulder, 3665 Discovery Drive, Boulder CO 80303, USA

ABSTRACT

Stellar flares are short-duration ($< \text{hours}$) bursts of radiation associated with surface magnetic reconnection events. Stellar magnetic activity generally decreases as a function of both age and Rossby number, R_0 , a measure of the relative dominance of the convective and rotational dynamos. However, without young stars have been overlooked in flare studies due to lack of long baseline observations and challenges with flare-detection methods. With this motivation, we select a sample of stars that are either (i) members, (ii) candidate members or (iii) have a high-probability of being members of 26 nearby young moving groups, clusters, or associations all known to be less than 300 Myr old that have been observed by the Transiting Exoplanet Survey Satellite (TESS) at 2-minute cadence. With this sample of 6,824 stars younger than 300 Myr, we identified 26,355 flares originating from 3,160 stars. Moreover, we robustly measured the rotation periods of 1,847 stars. We measure the flare frequency distribution (FFD) slope as a function of both age and spectral type and find the FFD slope, α , saturates for all spectral types at $\alpha = -0.5$ and is constant over the 300 Myr window studied here. Additionally, we find that R_0 and flare rate for stars $t_{\text{age}} = 100 - 300$ Myr are saturated out to $R_0 = 0.14$, which is consistent with other indicators of magnetic activity. We cross match our targets with *GALEX* and find no correlation between flare rate and Far- and Near-Ultraviolet flux. We compare the flare rates of planet hosting stars to comparable, larger samples of stars and find the majority of planet-hosting stars are relatively flare quiet. This may impact the atmospheric evolution of young short-period exoplanets. Finally, we detect evidence of stellar flare variations across five years of TESS data in eleven young stars, likely as a result of longer timescale stellar cycles.

1. INTRODUCTION

Stellar flares are the radiation component of magnetic reconnection events (). Such events are readily seen on the Sun (), particularly now as we enter a maximum in the solar cycle (). Such events can be used to understand the magnetic activity of other stars (). Additionally, by studying stellar flares we can understand how these short-duration events may impact exoplanet evolution (). While we cannot angularly resolve stellar flare events on other stars, we can detect and characterize

both spectroscopic and photometric signatures of such events. Spectroscopic characterization of stellar flares inform our understanding of non-thermal processes affiliated with such events, e.g. coronal mass ejections () or proton beams (). They can also inform our understanding of stellar plasma is displaced during these events ().

Photometric observations of stars are more readily available thanks to exoplanet transit discovery missions, and allow us to statistically characterize flare rates and energies. NASA's *Kepler*, *K2*, and the Transiting Exoplanet Survey Satellite (TESS) missions have provided a wealth of stellar variability data in addition to their primary objective of detecting transiting exoplan-

* NHFP Sagan Fellow

† NSF Astronomy and Astrophysics Postdoctoral Fellow

ets. Within time-series photometry, stellar flares can be identified by a sharp rise in the stellar flux and a subsequent exponential decay, corresponding to the cooling rate (). *Kepler* (Borucki et al. 2010) provided long-baseline high-cadence observations used to identify stellar flares. There has been extensive studies of flares in *Kepler* data, from the statistics of superflares on solar-type stars (e.g. Notsu et al. 2013; Shibayama et al. 2013; Maehara et al. 2015; Okamoto et al. 2021) to low-mass stars (e.g. Hawley et al. 2014; Silverberg et al. 2016). Davenport et al. (2019) found that flare activity decreased with increasing rotation period for 347 GKM stars. However, the flare frequency distribution (FFD) slope did not change significantly as a function of age. As a caveat, the ages of the stars were determined based on their rotation periods, relying on the assumption that gyrochronology alone accurately ages stars.

K2 provided 70-day baseline observations for a handful of young stars in groups such as Upper Scorpius, Pleiades, Hyades, and Praespe clusters. Ilin et al. (2019, 2021) analyzed flares K and M stars in these clusters and found that the overall flare activity decreased as a function of age. This relationship was steeper for more massive stars in the sample. Paudel et al. (2018) surveyed 10 M6 - L0 dwarfs observed with *K2* and found the L0 dwarf had a much shallower FFD than the M dwarfs. On average, they found that very young targets, defined by the tangential velocity of the star, overall had more flares.

More recently, TESS (Ricker et al. 2015) has provided near all-sky photometric observations at 30-minute cadence or less. Such an observing strategy has allowed for more detailed studies of young stellar flares from nearby young moving groups and associations, which are disperse in the sky (Gagné et al. 2018b). These new data have allowed for detailed studies of individual stars, for example characterizing eight superflares ($E_f > 10^{34}$ erg) on the young star AB Doradus over ~ 60 days of continuous observations (Schmitt et al. 2019).

The 11-year solar activity cycle represents a change in the magnetic activity of the Sun, and manifests itself in a variety of observables e.g., an increase in the total number of sunspots (Clette et al. 2014; Kilcik et al. 2014), an increase in the number of flares and coronal mass ejections (Crosby et al. 1993; Webb & Howard 1994; Lin et al. 2023), and an increase in the total solar irradiance (Lean 1987). The majority of insights we have gained in long-term activity cycles on other stars is through photometric monitoring and spectroscopic monitoring (Saar & Brandenburg 1999). Lehtinen et al. (2016) collected 16 to 27 years of B- and V-band photometry for 21 young active solar-type stars. They found evidence

of long-term stellar activity cycles in 18 targets following as $P_{\text{rot}}/P_{\text{cycle}} \propto R_0^{-1}$, where P_{rot} is the rotation period, P_{cycle} is the period of the stellar activity cycle, and R_0 is the Rossby number. Additionally, 50 years of spectroscopic observations of HD 166620 from the Mount Wilson Observatory and Keck revealed both a ~ 16 year periodicity in emission from the core of the Ca II H and K lines (Oláh et al. 2016) and evidence that this star entered a grand minima (Baum et al. 2022). A more complete review on the state of stellar activity cycles can be found by Jeffers et al. (2023) and Işık et al. (2023).

In addition to photometric and spectroscopic observations, solar flares trace the length of the solar activity cycle. The high-cadence observations from *Kepler* (4-year baseline) and TESS (currently 5-year baseline) are providing data sufficient for searching for stellar activity cycle from the variations in stellar flare rates. Davenport et al. (2020) demonstrated that the flare rate and FFDs of GJ 1234 has not changed appreciably over 10 years of observations with both *Kepler* and TESS. On the other hand, ? found that KIC 8507979, an M3V star, showed a clear decline in flare rate and change in FFD over 4-years of *Kepler* observations. While it is not expected to find flare rate and distribution variations in all stars given detection limitations, KIC 8507979 demonstrates the ability to study long-term flare variability as a potential tracer for stellar activity cycles.

The paper is presented as follows. In Section 2, we describe our sample, stellar flare identification and fitting methods, and methods for measuring stellar rotation periods. In Section 3, we present our flare-frequency distribution (FFD) fits as a function of stellar age, T_{eff} , and R_0 . In Section 4, we search for correlations in flare rates with FUV and NUV observations from *GALEX* and place the flare rates of young planet hosting stars in the context of our broader sample. We conclude in Section 5. We provide additional figures and tables in Section A.

2. TESS LIGHT CURVE CHARACTERIZATION

In this section, we provide an overview of the methodology associated with this paper. Specifically, we describe the sample selection in subsection 2.1, TESS light curve analysis in 2.2, flare identification in subsection 2.3, how we fit for flare parameters in 2.4, flare quality checks in 2.5, and measuring stellar rotation periods in 2.6.

2.1. Sample Selection

A primary goal of this paper is to measure the dependence of the stellar flare rates on stellar age. Particularly, we are interested in this dependency for stars

with ages $1 \leq t_{\text{age}} \leq 300$ Myr. To this end, we used the MOCA Data Base (Gagné et al. in prep.) to identify nearby young moving groups, associations, and open clusters with known ages which satisfied our criteria. From this database we identified 26 unique groups from which we created our sample of stars. The final selected targets were required to be: (i) confirmed members, (ii) high-likelihood candidate members, or (iii) candidate members. Membership to these groups has been primarily determined using kinematic information from *Gaia* (Gaia Collaboration et al. 2016, 2018). These rather stringent cuts resulted in a catalog of 30,889 stars across 26 associations. We summarize the sample and ages for each association (and therefore star) in Table 1.

Table 1. Adopted Ages of each Young Stellar Population and Number of Stars per Group

Population	Age [Myr]	N _{stars}	Ref.
AB Doradus	133^{+15}_{-20}	88	1
Blanco 1	$137.1^{+7.0}_{-33}$	428	2
Carina	45 ± 9	94	3
Carina-Musca	32	35	4
Chamaeleon	5	424	5
Columba	42	126	3
Greater Taurus Subgroup 5	8.5	56	4
Greater Taurus Subgroup 8	4.5	122	4
Lower Centaurus Crux	15	761	6
MELANGE-1	250^{+50}_{-70}	19	7
Octans	35 ± 5	64	8
Pisces Eridanis	120	219	9
Pleiades	$127.4^{+6.3}_{-10}$	1421	2
α Persei	$79^{+1.5}_{-2.3}$	625	2
IC 2602 system	$52.5^{+2.2}_{-3.7}$	160	2
NGC 2451A	48.5	59	4
Oh 59	162.2	62	10
Platais 9	50	124	11
RSG2	126	145	12
Theia 301	195	437	10
Theia 95	30.2	230	10
TW Hydrae	10	24	3
Upper Centaurus Lupus	16 ± 2	696	6
Upper Scorpius	10	106	6
Vela-CG4	33.7	299	4
Total		6,824	

NOTE—Age references: (1) Gagné et al. (2018a); (2) Galindo-Guil et al. (2022); (3) Bell et al. (2015); (4) Kerr et al. (2021); (5) Luhman (2007); (6) Pecaut & Mamajek (2016); (7) Tofflemire et al. (2021); (8) Murphy & Lawson (2015); (9) Curtis et al. (2019); (10) Kounkel et al. (2020); (11) Tarricq et al. (2021); (12) Röser et al. (2016)

2.2. TESS Light Curves

As described in the previous subsection, we select stars in our sample for which TESS light curves have been obtained with 2-minute cadence. The reason for doing this is so that we are able to resolve and accurately measure the properties of flares for each of these stars (Howard & MacGregor 2022). We cross-matched our sample obtained with the MOCA Database with the TESS Input Catalog (TIC) based on their Gaia DR2 RA and Dec. We required that the distance between the target and the nearest TIC target was within $< 1''$.

This process provided a final sample of 6,824 unique targets. These targets have each been observed at a 2-minute cadence between TESS Sector 1 and Sector 67; Sector 67 was the latest available sectors at the time that this analysis was performed. In Figure 1, we show the distribution of the on sky positions and effective temperatures, T_{eff} , of the final sample. We use T_{eff} as our stellar characterization metric over the standard M_{\star} because ~ 600 stars in our sample are lacking mass information in the TIC. It is evident that many targets exhibit strong tendency for proximity towards the northern and southern ecliptic poles (Figure 1). Therefore, many of these targets were observed over multiple sectors. The entirety of the available data yielded 17,964 light curves processed by the Science Processing Operations Center (SPOC) pipeline (Jenkins et al. 2016). Our sample has an average of ~ 3 light curves per target (although with significant spread across targets). For our analysis, we used the SPOC-processed SAP_FLUX.

2.3. Flare Identification

Once we had the light curves for each target, we performed the following procedure to identify stellar flares. First, we implemented the machine learning flare-identification methods presented and described in Feinstein et al. (2020). This method relies on the fact that all flare events have similar time-dependent morphologies. These flare-profiles can generally be described as a sharp rise followed by an exponential decay in the white light curve. This identification-technique implements the convolutional neural network (CNN), *stella* (Feinstein et al. 2020). The neural network was trained to identify flare events in TESS 2-minute data using a catalogue of flare events from TESS Sectors 1 and 2 that were validated by-eye (Günther et al. 2020).

There are many benefits to using the CNN for stellar flare identification. Primarily, the CNN is advantageous because it is insensitive to the stellar baseline flux. This feature inherently stems from the fact that the network

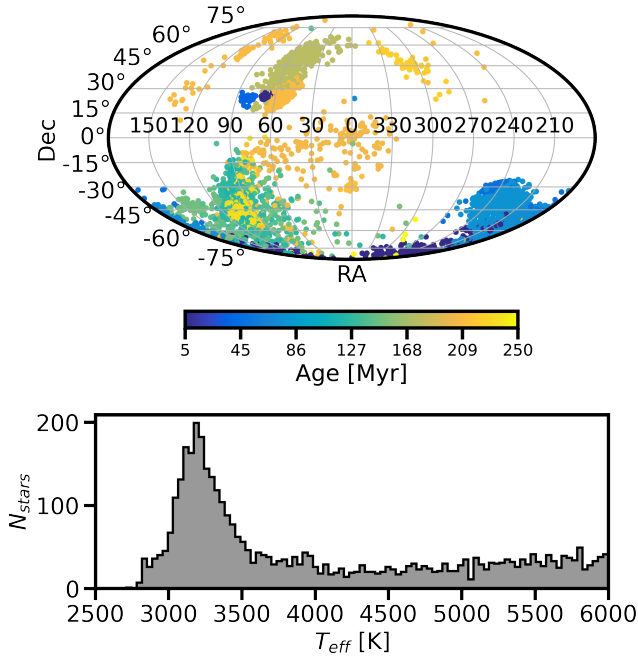


Figure 1. Top: Distribution of our selected sample across the sky and colored by the adopted age of the association (see Table 1). The all-sky coverage by TESS has unlocked new populations of stars to observe. We take advantage of this observing strategy to measure flare rates across 26 different nearby young moving groups, clusters, and associations. Bottom: Distribution of adopted effective temperatures, T_{eff} [K] for stars in our sample. We include all stars with $T_{\text{eff}} \leq 6000$ K.

is trained to search *only* based on flare morphology. It is therefore relatively insensitive to the absolute flux levels, so long as the inherent noise does not overwhelm the signal itself. This means that rotational modulation peaks — which are themselves driven by stellar heterogeneities — are not accidentally identified as flares. This is especially advantageous for our sample of young stars, which readily exhibit rotational modulation in their light curves.

Based on these advantages, the final compiled sample of flares is *unbiased* towards low-amplitude/low-energy flares. It is important to note that these low-energy events are typically not identified in traditional sigma-outlier identification methods (Chang et al. 2015). The *stella* CNN models calculates the probability that a data point in a light curve is associated with a flaring event. Specifically, it takes the light curve (time, flux, flux error) as an input and returns an array with values of [0,1], which are treated as the probability a data point is (1) or is not (0) part of a flare. We ran every light curve through 10 independent *stella* models and averaged the outputs to ensure that our statistics were accurate. We note that in this processing, the CNN ig-

nores 200-minutes before and after any gaps in the data. Therefore, any flares which occur during these times are not identified.

In order to identify a single flare event, the *stella* code uses the predictions per data point to group together points. We modified this stage of identification slightly from the original flare-identification method. Specifically, we identified all data points with a probability of being associated with a flare of $P > 0.75$. Any data points that were within 4 cadences of each other were considered to be a single flare event. We did not consider any potential flares that had three or fewer points with $P > 0.75$. This was motivated by the fact that sometimes a single-point outlier is assigned a high probability of being a flare. Therefore, we neglected these events. We assigned the probability of the whole flare event as the probability of the peak data point.

2.4. Modeling Flare Properties

As described in the previous subsection, flares are well-described in light curves as a sudden increase in flux followed by an exponential decay. For this paper, we used the analytical flare model, Llamaradas Estelares which was presented in Tovar Mendoza et al. (2022)¹, to fit the flares and extract the flare parameters in all of the light curves of our sample. This model builds upon the model presented in Davenport et al. (2014). Specifically, it includes the convolution of a Gaussian with a double exponential model in the flare profile.

The analytical model is robust in that it is able to accounts for multiple inherent features of flares. Specifically, it can incorporate the flare (i) amplitude, (ii) heating timescale, (iii) rapid cooling phase timescale, and (iv) slow cooling phase timescale. We implemented a nonlinear least squares optimization to fit for the time of the flare peak (t_{peak}), full width at half maximum (FWHM), and the amplitude (A) of each flare in the sample. We combine the model with a second-order polynomial fit to a 1.2-hour baseline before and after the flare during only the fitting stage. This was implemented in order to account for any slope due to rotational modulation, and therefore was particularly relevant for the rapid rotators ($P_{\text{rot}} < 2$ days).

We calculated the equivalent duration, ED, of the flare by integrating the quiescent-normalized flare flux with respect to time. We calculate the flare energy, E_{flare} , using,

$$E_{\text{flare}} = L_{\star} A \text{ED} s. \quad (1)$$

¹ <https://github.com/lupitator/Llamaradas-Estelares>

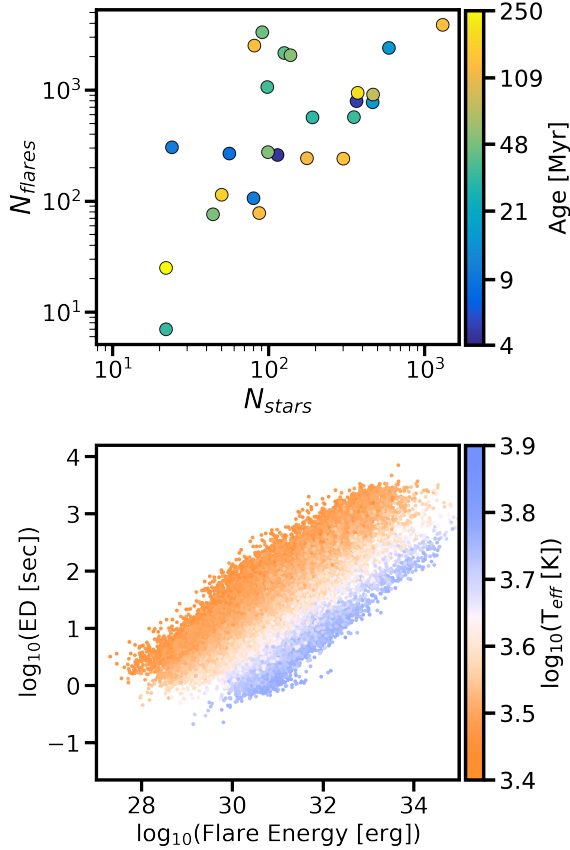


Figure 2. High level summary of the demographics of flares in our sample. Top: The number of flares identified compared to the number of stars in each nearby young moving group, cluster, or association. A one-to-one relationship is expected. Middle: The distribution measured TESS energies and equivalent durations of flares in our sample, colored by the probability of the flare as identified with *stella*. Bottom: Same as the middle plot, except colored by the T_{eff} [K] of the star. We limit our sample to stars with $T_{\text{eff}} \leq 6000$ K.

In Equation 1, L_* is the luminosity of the star and s is a scaling factor defined as $s = B_\lambda(T_{\text{eff}})/B_\lambda(T_{\text{flare}})$, where $B_\lambda(T)$ is the Planck function. We assume that the flare temperature is 9000 K (Kretzschmar 2011). Although 900

2.5. Flare Quality Checks

In this subsection, we describe the methodology we employ to ensure that flares identified by the CNN are high quality. The *stella* CNNs were trained on data from TESS Sectors 1 and 2. However, the noise properties are variable across sectors in TESS data. The CNNs are therefore unable to accurately account for and capture this variation when operating on different sectors. Moreover, the original CNNs were only trained on a sample of 1,228 stars. This sample does not necessarily encapsulate all or even a sufficient distribution of variable

stars types, such as eclipsing binaries, RR Lyraes, and fast rotators with rotation periods $P_{\text{rot}} < 1$ day. We therefore apply additional quality checks to ensure our flare sample has little to no contamination from other sources.

Specifically, we remove flares from our sample which did not satisfy one or more of the following criteria.

1. The amplitude of the flare must be > 0.01 , or 1%. This follows the limits set by Feinstein et al. (2020).
2. The flare amplitude must be at least twice the standard deviation of the light curve 30 minutes before and 45 minutes after the flare. This ensures that the feature is not a sharp noise artifact.
3. The fitted flare model parameters must be physically motivated: $\text{FWHM} > 0$; $A > 0$; $\text{ED} > 0$.
4. The flare parameters must be $\sigma_A < 0.5$ and $\sigma_{t_{\text{peak}}} < 0.01$.

We find that when the errors on the first and fourth criteria are larger than the cut-offs, the flares are often simply mischaracterized noise.

As a final check, we performed an exhaustive by-eye verification of flares from light curves for stars with flare rates, $\mathcal{R} > 1 \text{ day}^{-1}$. These stars generally tend to have $T_{\text{eff}} > 5000$ K and TESS magnitudes < 8 . Therefore, their light curves are dominated by sharp noise which *stella* often mischaracterizes as flares. As a final cut, the sample only includes events that have a probability $P \geq 98\%$ of being a true flare. After performing these additional checks, we obtain a final flare sample of 26,355 flares originating from 3,160 stars (Figure 2).

2.6. Measuring Rotation Periods

In addition to understanding flare statistics across young stars, we measure the rotation periods, P_{rot} of stars in our sample and search for correlations between P_{rot} and Rossby number, R_0 . Seligman et al. (2022) demonstrated that stars with low Rossby numbers $R_0 < 0.13$ exhibit shallower flare frequency distribution slopes. These shallower slopes are caused by an excess of high energy flares compared to lower energy flares originating from these sources.

In order to perform this, we describe how we measure stellar rotation periods from the TESS light curves. To this end we used *michael*², an open-source Python package that robustly measures P_{rot} using a combination traditional Lomb-Scargle periodograms and wavelet

² <https://github.com/ojhall94/michael>

transformations (Hall et al. submitted). `michael` measures P_{rot} using the `eleanor` package, which extracts light curves from the TESS Full-Frame Images (FFIs; Feinstein et al. 2019).

We ran `michael` on all stars in our samples from which flares were identified. The estimated rotational periods were subsequently vetted by-eye with the `michael` diagnostic plots. This vetting was implemented to ensure that the measured P_{rot} was not a harmonic of the true P_{rot} or that the period is from an occulting companion. In total, we robustly measured rotation periods for 1,847 stars. Additionally, we identified 17 eclipsing binaries or potentially new planet candidates.

3. FLARE RATES OF YOUNG STARS

In this section, we use the previous methodology to estimate the flare rates of the young stars in our sample. We implement three main steps in this analysis. First, we perform the standard FFD fitting of a power-law to the distribution of flare energies described in subsection 3.1. Next, to determine if there is a correlation between R_0 and flare distributions we fit a truncated power-law to the distribution of flare amplitudes in subsection 3.3. Finally we fit the relationship between R_0 and flare rates in subsection 3.2.

The number of stars, and consequently the number of flares in each association varied greatly (Figure 2). This was primarily caused by the limited number of stars that had been observed at 2-minute cadence in TESS. We therefore did not measure FFD properties as a function of association. Instead, we group stars by T_{eff} and average adopted association age.

We define the following spectral type bins by T_{eff} :

- M-stars below the fully convective boundary ($T_{\text{eff}} = 2300 - 3400$ K)
- early type M-stars ($T_{\text{eff}} = 3400 - 3850$ K)
- late K-stars ($T_{\text{eff}} = 3850 - 4440$ K)
- early K-stars ($T_{\text{eff}} = 4440 - 5270$ K)
- G-stars ($T_{\text{eff}} = 5270 - 5930$ K)

We did not include any stars hotter than $T_{\text{eff}} > 5930$ K. These hot stars generally exhibit light curves dominated by noise in the TESS observations. Additionally, we grouped stars in the following age space: 4 – 10 Myr (including Upper Scorpius and TW Hydrae), 10 – 20 Myr, 20 – 40 Myr, 40 – 50 Myr, 70 – 80 Myr, 120 – 150 Myr, and 150 – 300 Myr. We note that there is a gap in age from 50 – 70 Myr, which could be expanded with the identification of more associations in this age range.

3.1. Standard Power-Law Fits

We fit the stars FFD slopes, approximated as a power-law, using the T_{eff} and age bins described above. Flares were binned into 25 bins in log-space from $10^{27} - 10^{35}$ erg. We perform the FFD fits using the energy bin with the maximum flare rate as the base level, and then with all flare energies higher than that. We perform this cut because lower energy bins may be incomplete, exhibiting a turnover in the FFD at lower energies. Moreover, the energy turnover in the FFD cannot be accurately modeled as a power-law.

We fit the FFD using the MCMC method implemented in `emcee` (Goodman & Weare 2010; Foreman-Mackey et al. 2013). Specifically, we fit for the slope, α , y-intercept, b , and an additional noise term, f . This noise term accounts for an underestimation of the errors in each bin. We initialized the MCMC fit with 300 walkers and ran our fit over 5000 steps. We discarded the first 100 steps upon visual inspection, after which the steps were fully burned-in.

The full FFDs are presented in Figure A1, along with 100 samples from the MCMC fit. The measured FFD slopes, α , are presented in Figure 3. We approximate the error on the slope as the lower 16th and upper 84th percentiles from the MCMC fit.

There is a $1 - 3\sigma$ discrepancy between the FFD slope measured in Ilin et al. (2021) and the work presented here at ages ~ 120 Myr (α ranges from -1.32 ± 0.19 to -0.91 ± 0.18 , depending on the T_{eff} bin). Ilin et al. (2021) used the *K2* 30-minute light curves for their analysis, compared with our TESS 2-minute light curves. Additionally, our sample has $\sim 2\times$ the number of stars and $\sim 7\times$ the number of flares than Ilin et al. (2021). First, we test if these differences are driven by differences in sample binning. We reevaluate the FFDs assuming the T_{eff} bins presented in Table 3 of Ilin et al. (2021). We find α remains consistent with our presented values to within $\sim 1\sigma$ of the nearest temperature bin. Second, we reevaluate the FFDs assuming the total number of flares fit in Ilin et al. (2021). Our sample has $\sim 2\times$ the number of stars and $\sim 7\times$ the number of flares than their sample. We draw n_{fit} , Ilin et al. (2021) (last column in Table 3 of Ilin et al. 2021) flares from our sample 100 times without replacement, refit the FFD, and take the average FFD slope from that sub-sample of flares to our results. We find α remains consistent with our presented values to $\sim 2\sigma$. We note that in most cases n_{fit} , Ilin et al. (2021) $< n_{\text{fit}}$, this work. Therefore, the increased disagreement in α could be due to smaller sample sizes.

Additionally, we test if the difference in α is driven by the cadence differences between *K2* (30-minute) and

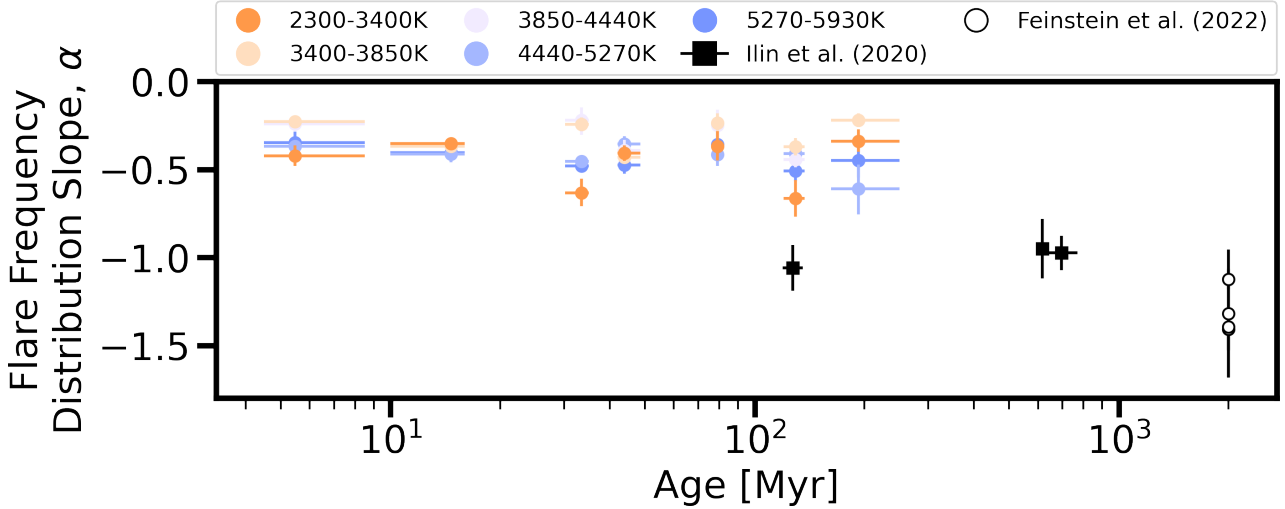


Figure 3. Measured flare-frequency distribution slopes, α , as a function of stellar effective temperature, T_{eff} and age. We measured these FFDs with respect to flare energy. We find the FFD slopes as a function of energy are consistent with $\alpha = -0.6$ to -0.2 for stars < 300 Myr in TESS observations. A shallower FFD slope is indicative of more high-energy flares. We present all measured FFDs in Figure A, and all measured slopes and errors in Table ???. We find the shallowest slopes for stars $T_{\text{eff}} = 3400 - 4440$ K, with a range from $\alpha = -0.44$ to -0.22 . We do not include the results for stars $T_{\text{eff}} = 3850 - 4440$ K and $t_{\text{age}} = 20 - 40$ Myr as this bin contained only six stars with detected flares. We present the average results of measured FFD slopes for the Hyades, Pleiades, and Praesepe clusters from Ilin et al. (2021) as black squares. We present the results of measured FFD slopes for all TESS primary mission targets in white circles (Feinstein et al. 2022). We present these data as “field-age”. We discuss what drives the difference between our sample and Ilin et al. (2021) in Section 3.1.

TESS (2-minute). We bin all of the flares in our sample down the 30-minute cadence, re-fit for flare A and ED , and recalculate the flare energy. We re-fit the FFD for this altered sample and measure an FFD slopes consistent to $\sim 1\sigma$ with our presented in this work. Therefore, the discrepancy seen here is not driven by observational differences between $K2$ and TESS.

Finally, we test if the differences are driven by the energy ranges fit over. The CNN-based flare detection algorithm has previously been demonstrated to be less-biased against lower energy flares. Like this work, Ilin et al. (2021) fits the FFD across flare energies which are not affected by a reduced efficiency in the low-energy flare detection. In energy space, these fits begin between $E_f = 10^{32-33}$ erg, compared to our fits which begin between $E_f = 10^{31-32}$ erg (Figure A). When we limit our sample to $E_f \geq 10^{32.5}$ erg, we find the FFD slopes become *steeper* and more consistent with *alpha* presented in Ilin et al. (2021). Therefore, the difference in α between this work and Ilin et al. (2021) for stars with $t_{\text{age}} = 120 - 150$ Myr is driven by the lower energy flares, with which we are more complete to with TESS than $K2$.

The measured FFD slopes are shallower than those measured using smaller samples of young stars. Jackman et al. (2021) fit the three FFDs for M3-M5, M0-M2, and K5-K8 stars younger than 40 Myr that had been

observed with Next Generation Transit Survey. They measured slopes of 0.94 ± 0.04 , 0.69 ± 0.05 , 0.82 ± 0.14 per bin, which each contained ≤ 120 flares. It is also worth noting that the slopes measured here are based on up to an order of magnitude more flares per fit.

3.2. Flare Rate Dependence on Rossby Number

The Rossby number, R_0 , is a parameter which marginalizes over several properties which are known to affect the stellar dynamo, such as the rotation period and stellar mass. Specifically, in the context of stellar dynamo the Rossby number indicates the dominance of the convective versus rotational dynamo. It is defined as $R_0 = P_{\text{rot}}/\tau$, where τ is the convective turnover time. We convert our measured rotation periods to R_0 , approximating τ following the prescription in Wright et al. (2011). We equate the flare rates, \mathcal{R} , for individual stars as

$$\mathcal{R} = \frac{1}{t_{\text{obs}}} \left(\sum_{i=1}^N p_i \right). \quad (2)$$

In Equation (2), \mathcal{R} is the flare rate in units of day^{-1} , t_{obs} is the total amount of time a target was observed with TESS, and p_i is the probability that flare i is a true flare as assigned by *stella*. We compare the calculated R_0 to measured flare rates for all stars we measured P_{rot} for. The results are presented in Figure 4.

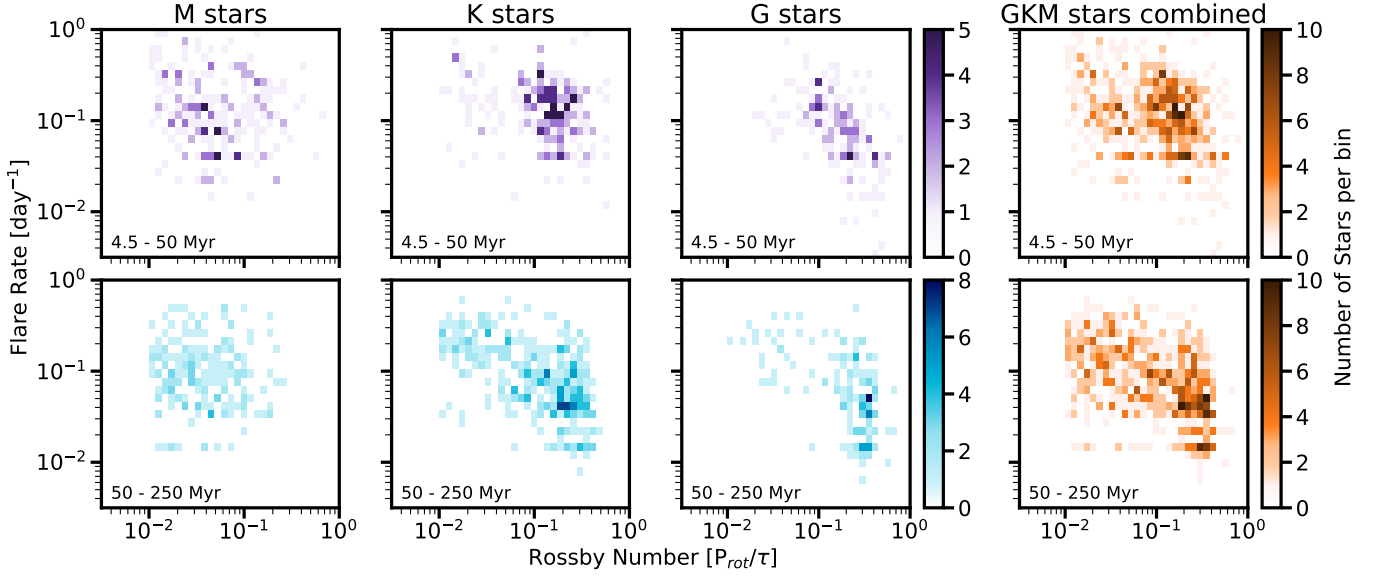


Figure 4. Comparison of Rossby Number, R_0 and flare rate for young GKM stars. We find no change in the average flare rate for GKM stars < 250 Myr. We see evidence that as R_0 increases, the average flare rate decreases. This is similar to results presented in Medina et al. (2020), however our sample extends this trend to young GKM stars, while previous results were limited to nearby M dwarfs. The top row are stars with ages 4.5 – 50 Myr; the bottom row are stars with ages 50 – 250 Myr. The histograms are colored by number of stars in each bin.

From these results, we are able to evaluate the dependence of the flare rate on age, spectral type, and R_0 . We split the sample between stars younger and older than 50 Myr. This age roughly correlates to the age at which GKM stars turn onto the main sequence. The flare rate of stars younger than 50 Myr slightly decreases with increasing R_0 . However, there is a significant amount of scatter in this relationship.

As can be seen by comparing the upper and lower panels in Figure 4, the flare rate dependence on Rossby number is most evident in older, more massive stars between 50 – 300 Myr. For M stars, we see minimal evolution in both the average flare rate and R_0 between the two samples. For K stars, R_0 evolves more dramatically during the first 250 Myr while the scatter in the flare rate decreases. For G stars, the scatter in R_0 decreases and the average flare rate across the sample decreases. We present a compiled histogram for all stars in our sample in the right column of Figure 4.

To better understand this trend, we fit three functions to the flare rate Rossby number parameter space: (i) a constant value, (ii) a single power law, and (iii) a piece-wise function consisting of a constant value and a power law. We computed the χ^2 between each of these fits and the data. For (iii), we fit for where the R_0 turnover should occur by computing the χ^2 across a range of $R_0 = [0.09, 0.18]$. We weighted the data points based on the density of points in a given bin (Figure 4). For stars 4.5 – 50 Myr, we find the distribution is best-fit with a

single power law with slope $m = -0.102 \pm 0.018$ and y-intercept $b = -0.660 \pm 0.017$. For stars 50 – 250 Myr, we find the distribution is best-fit with a piece-wise function of the form

$$\mathcal{R} = \begin{cases} C & R_0 \leq 0.136 \\ 10^b * R_0^m & R_0 > 0.136 \end{cases} \quad (3)$$

In Equation (3), \mathcal{R} is the flare rate, $C = 0.269 \pm 0.007$, $m = -0.612 \pm 0.039$, and $b = -1.113 \pm 0.035$. The location of the turnover is consistent with what has been measured in other observations of magnetic saturation for partially and fully convective stars (e.g. L_X/L_{bol} ; Wright et al. 2018).

A similar relationship was discussed in Davenport (2016). With a sample of 851,168 flares detected in both *Kepler* 1- and 30-minute cadence data, Davenport (2016) found that the relationship between Rossby number and relative flare luminosity could be fit by a broken power law, with a break at $R_0 = 0.03$ and a slope of ~ -1 dominating higher R_0 . While the metrics used between Davenport (2016) and this paper are different, both suggest a saturation in flares for stars with low R_0 . Additionally, Medina et al. (2020) found a broken power-law relationship between R_0 and the flare rate for flares with $E_f > 3.16 \times 10^{31}$ erg, the sample’s completeness threshold. Medina et al. (2020) analyzed light curves of 419 low-mass ($M_* = 0.1 - 0.3 M_\odot$) main-sequence stars in the Solar neighborhood as observed by TESS. This study found that the flare rate saturates

at $\log(\mathcal{R}) = -1.30 \pm -0.08$ for $R_0 < 0.1$ and rapidly declines for $R_0 > 0.1$. While neither of these previous studies allow for a direct comparison to our results, given the differences in sample selection, all point towards evidence of flare rate saturation for stars with low R_0 and a steep drop-off in flare rate for stars with higher R_0 .

3.3. Truncated Power-Law Fits

We search for evidence of variations of the FFDs as a function of Rossby number, R_0 . This is motivated by the data presented in Seligman et al. (2022). In that work, they modeled flares driven by magnetic reconnection events driven by rotational forces as well as convective dynamo. Seligman et al. (2022) found that stars with $R_0 < 0.13$ exhibited shallower FFD slopes than stars with $R_0 \geq 0.13$ to several sigma significance. The differences in the FFDs were indicative of relatively more high-energy flares to low-energy flares. This was interpreted as evidence of a more dominant rotational dynamo compared to the convective dynamo, which preferentially produced longer magnetic braids in the stellar coronae.

In this subsection, we test this theory with a much larger sample of stars (1,847 instead of 807 stars). We fit the distributions separated by the fitted R_0 presented in Section 3.2. In order to perform the fits, we follow the prescription described in greater detail in Seligman et al. (2022). Here, we provide a brief summary of the prescription. Specifically, we fit a truncated power-law distribution of the form,

$$dp/dA \propto A^{-\alpha_T} e^{-A/A_*}. \quad (4)$$

In Equation (4), A is the amplitude of the flare, A_* is a flare amplitude cutoff parameter and α_T is the slope, rather than α . We fit the slopes using the MCMC method implemented in emcee (Goodman & Weare 2010; Foreman-Mackey et al. 2013). We used the log-likelihood function in Seligman et al. (2022) and fit for A_* and α_T . We initialized the MCMC fit with 200 walkers and evaluated the fit over 5000 steps. The first 1000 steps were discarded upon visual inspection. The results are presented in Figure 5.

We find that stars with $R_0 \leq 0.136$ have a best-fit slope of $\alpha_T = 1.076 \pm 0.020$, while stars with larger R_0 have a best-fit slope of $\alpha_T = 1.604 \pm 0.040$. fill out more.

4. DISCUSSION

4.1. Correlations with Far- and Near-Ultraviolet Flux

X-ray luminosity surveys of stars have revealed a saturation limit with respect to the star’s rotation period. Namely, there is no evolution in L_X/L_{bol} for stars with $P_{\text{rot}} < 10$ days (Pizzolato et al. 2003).

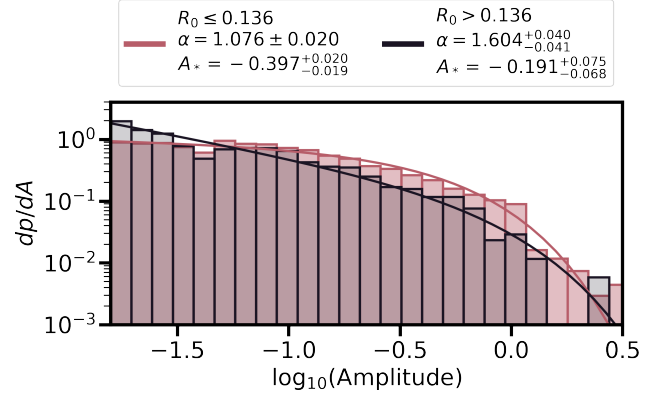


Figure 5. Flare frequency distributions, as a function of flare amplitude, for stars with $R_0 \leq 0.12$ (red) and stars with $R_0 > 0.12$ (black). We present the best-fit model, and the best-fit values of the model slope and normalization factor in the legends. Our sample of $R_0 \leq 0.12$ includes 13,132 flares from 800 stars; our sample of $R_0 > 0.12$ includes 5,603 flares from 747 stars. We find the stars with smaller Rossby numbers have shallower slopes, consistent with more, high-energy flares and potentially larger convective regions (Seligman et al. 2022).

The Far- and Near-Ultraviolet (FUV/NUV) is another tracer of magnetic activity. Young stars are known to have excess luminosity in both of these wavelengths (). We use archival observations from the *Galaxy Evolution Explorer* (GALEX; Martin et al. 2005) to search for trends in FUV/NUV saturation and flare rate saturation. GALEX provides broad FUV photometry from 1350 – 1750Å and NUV photometry from 1750 – 2750Å. We crossmatch our targets with the GALEX catalog. We follow the sample selection methods outline in (Schneider & Shkolnik 2018). We search a 10'' radius around the coordinates of each target in our sample. We include targets with no bad photometric flags (e.g. fuv_artifact or nuv_artifact == 0) as defined in the catalog. This is recommended by the GALEX documentation, as flags could be assigned due to bright star window reflection, dichroic reflection, detector run proximity, or bright star ghost. We exclude targets with measured magnitudes brighter than 15, which marks the saturation limit for both the FUV and NUV photometers (Morrissey et al. 2007).

Based on these thresholds, we find that 462 stars in our sample have NUV photometry and 139 stars have FUV photometry. We explore if flare rate saturation and FUV/NUV saturation are correlated with the derived R_0 per star. We present our results in Figure 6. We present the measured FUV/NUV flux normalized by the J-band flux of the star, since it is the fractional flux which acts as an activity indicator. While bolometric lu-

minosities would be a better normalizing factor, we find the majority of stars in our target do not have this parameter measured. To assess FUV/NUV correlations in a larger statistical sense, we thus keep the normalization to f_J .

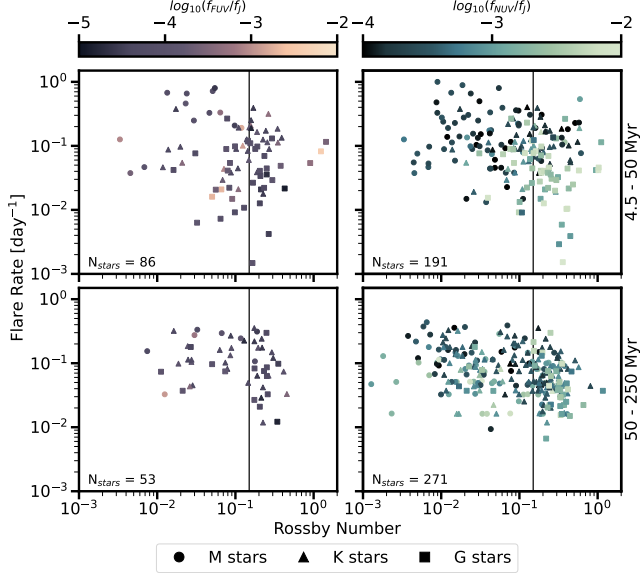


Figure 6. Calculated FUV (left) and NUV (right) GALEX flux for stars in our sample. We normalize these values by the J-band flux of the star. We find no strong correlation between the NUV/FUV flux and the measured flare rate or Rossby number. The top row shows GKM stars < 50 Myr; the bottom row shows GKM stars \geq 50 Myr. M stars are shown as circles, K stars as triangles, and G stars as squares. We note that f_{NUV} traces the photosphere of GK stars, and therefore may not be the best comparison bandpass when looking for trends in magnetic activity.

4.2. Comparison to Young Planet Host Stars

The all-sky observing strategy of TESS has revealed a new population of young transiting exoplanets. Characterizing the local environment for these planets is crucial to understanding their subsequent evolution to forming the mature population of planets. It is debated whether stellar flares are beneficial or detrimental to exoplanets. On one hand, **creates life**. On the other hand, stellar flares and affiliated coronal mass ejections can permanently alter atmospheric compositions (Chen et al. 2021) and increase the amount of atmospheric mass stripped during the early stages of planet evolution (Feinstein et al. 2020). To understand the evolution of these new insightful young transiting exoplanets, we compare their measured flare rates to a more statistical sample of stars with similar ages and T_{eff} .

We measured the flare rates of planet hosting stars < 300 Myr, comparable to the ages of our primary sam-

ple. We followed the methods outlined in Section 2 to detect and vet flares. For each star, we created an equivalent sample with respect to both age and T_{eff} to compare the flare rates too. We considered stars with ages ± 30 Myr of the planet hosting star and $T_{\text{eff}} \pm 1000$ K. We calculate the flare rate following Equation 2. We present the flare rates of planet-hosting stars and a comparable sample of stars in Figure 7 and report the measured rates in Table 2. For the comparable sample, we report the median flare rate, and the lower 16th and upper 84th percentiles.

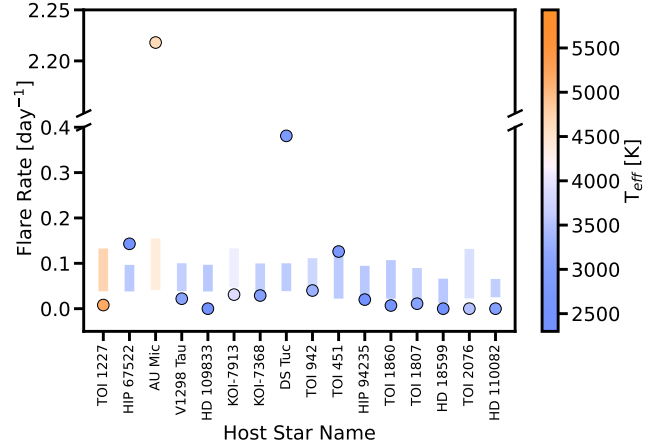


Figure 7. Comparison of flare rates from young planet host stars with respect to a comparable sample with respect to age [Myr] and T_{eff} [K]. Circles represent the flare rate of the host star (name along the x-axis); vertical bars represent the lower 16th and upper 84th percentiles for the comparable sample. The majority of young planet hosting stars have flare rates towards the lower end of the comparable sample's distribution. A handful of hosts have more flares, including HIP 67522, AU Mic, DS Tuc A, and TOI 451. We find no correlation between age or T_{eff} that may result in young planet hosts having more or fewer flares than a larger comparable sample. The measured flare rates are presented in Table 2.

4.3. Evidence of Stellar Cycles

The Sun goes through a 12-year solar cycle, which oscillates between times of high and low activity. The solar cycle manifests itself in a variety of observables, including a change in the flare rate, by a factor of 10 (), and the flare energies released (). Constraints of stellar cycles have predominantly relied on photometry (see recent review by ?). However, tracing stellar cycles via stellar flares may be more reliable, as flares are a direct consequence of magnetic activity. explored measuring the stellar cycle length of KIC 8507979, a star in the *Kepler* field which was observed for 18 90-day quarters.

Table 2. Young Planet Host Flare Rates

Host Name	Age	Flare Rate	Comp. Sample
	[Myr]	[day ⁻¹]	Flare Rate [day ⁻¹]
TOI 1227	11 ± 2	0.008	0.119 ^{+0.148} _{-0.046}
HIP 67522	17 ± 2	0.169	0.046 ^{+0.069} _{-0.020}
AU Mic	22 ± 3	2.218	0.133 ^{+0.171} _{-0.046}
V1298 Tau	23 ± 4	0.022	0.074 ^{+0.091} _{-0.033}
HD 109833	27 ± 3	0.000	0.046 ^{+0.070} _{-0.020}
KOI-7913	36 ± 10	0.031	0.134 ^{+0.162} _{-0.045}
KOI-7368	36 ± 10	0.029	0.064 ^{+0.087} _{-0.030}
DS Tuc	45 ± 4	0.420	0.056 ^{+0.078} _{-0.024}
TOI 942	50 ⁺³⁰ ₋₂₀	0.040	0.086 ^{+0.117} _{-0.038}
TOI 451	120 ± 10	0.128	0.071 ^{+0.085} _{-0.029}
HIP 94235	133 ⁺¹⁵ ₋₂₀	0.020	0.051 ^{+0.079} _{-0.017}
TOI 1860	133 ± 26	0.008	0.067 ^{+0.086} _{-0.025}
TOI 1807	18040	0.013	0.060 ^{+0.085} _{-0.022}
HD 18599	200 ⁺²⁰⁰ ₋₇₀	0.000	0.025 ^{+0.044} _{-0.015}
TOI 2076	204 ± 50	0.000	0.092 ^{+0.091} _{-0.045}
HD 110082	250 ⁺⁵⁰ ₋₇₀	0.000	0.047 ^{+0.067} _{-0.020}

They found the flare rate decreased over each quarter, which could be fit by $L_{\text{fl}}/L_{\text{Kp}} = (-9.96 \pm 3.94) \times 10^{-2} \times t_{\text{yr}} + (2.43 \pm 0.11)$, where t_{yr} is the time in years, and $L_{\text{fl}}/L_{\text{Kp}}$ is a parameterization of the *Kepler* flare rate as defined by (Hawley et al. 2014).

It is possible that the length of the stellar cycle is related to the P_{rot}/R_0 of the star as ... (). If this is the case, then stars with P_{rot} will have shorter stellar cycle lengths. The TESS Extended Mission has provided a five-year baseline, similar to *Kepler*, although the sampling is sparser. Within our sample of fast rotators, we searched for evidence of stellar cycles. Our sample contains 31 stars which have been observed for $t_{\text{obs}} \geq 400$ days and $n_{\text{flare}} > 100$.

We search for evidence of changes in the stellar magnetic activity by looking at (i) the maximum flare energy in a given period of time and (ii) the flare rate over that same period of time. We grouped our observations by year observed, even if the star was not continuously observed throughout that year.

5. CONCLUSIONS

In this work, we present the first measured flare rates for stars < 300 Myr using TESS 2-minute cadence observations. We identified originating 28,822 flares from 3,983 stars. The results of our work are summarized as follows:

1. We measured the flare-frequency distribution (FFD) slope, α , for samples of flares binned by age and T_{eff} . We find α saturates at $\alpha = -0.5$ for stars younger than 300 Myr and declines after that age. This is the first evidence that, like other tracers of stellar magnetic activity, flare rates saturate across spectral types.
2. We measured the y-intercept, β , for the same bins of flares. We find that ...
3. We measured the rotation periods, P_{rot} for **n** stars in our sample using the open-source Python package **michael**.
4. We measured the slope of a truncated power-law, α_T , for the same bins of flares. Additionally, we measured α_T as a function of Rossby number, R_0 .

We thank Darryl Seligman and David Wilson for thoughtful insights and useful conversations. This work made use of the open-source package, *showyourwork!* (Luger et al. 2021), which promotes reproducible publications. ADF acknowledges funding from ...

APPENDIX

A. SUPPLEMENTAL MATERIAL

Miscellaneous figures and such that people might want but I don't need to show

REFERENCES

- Baum, A. C., Wright, J. T., Luhn, J. K., & Isaacson, H. 2022, *AJ*, 163, 183, doi: [10.3847/1538-3881/ac5683](https://doi.org/10.3847/1538-3881/ac5683)
- Bell, C. P. M., Mamajek, E. E., & Naylor, T. 2015, *MNRAS*, 454, 593, doi: [10.1093/mnras/stv1981](https://doi.org/10.1093/mnras/stv1981)
- Borucki, W. J., Koch, D., Basri, G., et al. 2010, *Science*, 327, 977, doi: [10.1126/science.1185402](https://doi.org/10.1126/science.1185402)
- Chang, S. W., Byun, Y. I., & Hartman, J. D. 2015, *ApJ*, 814, 35, doi: [10.1088/0004-637X/814/1/35](https://doi.org/10.1088/0004-637X/814/1/35)

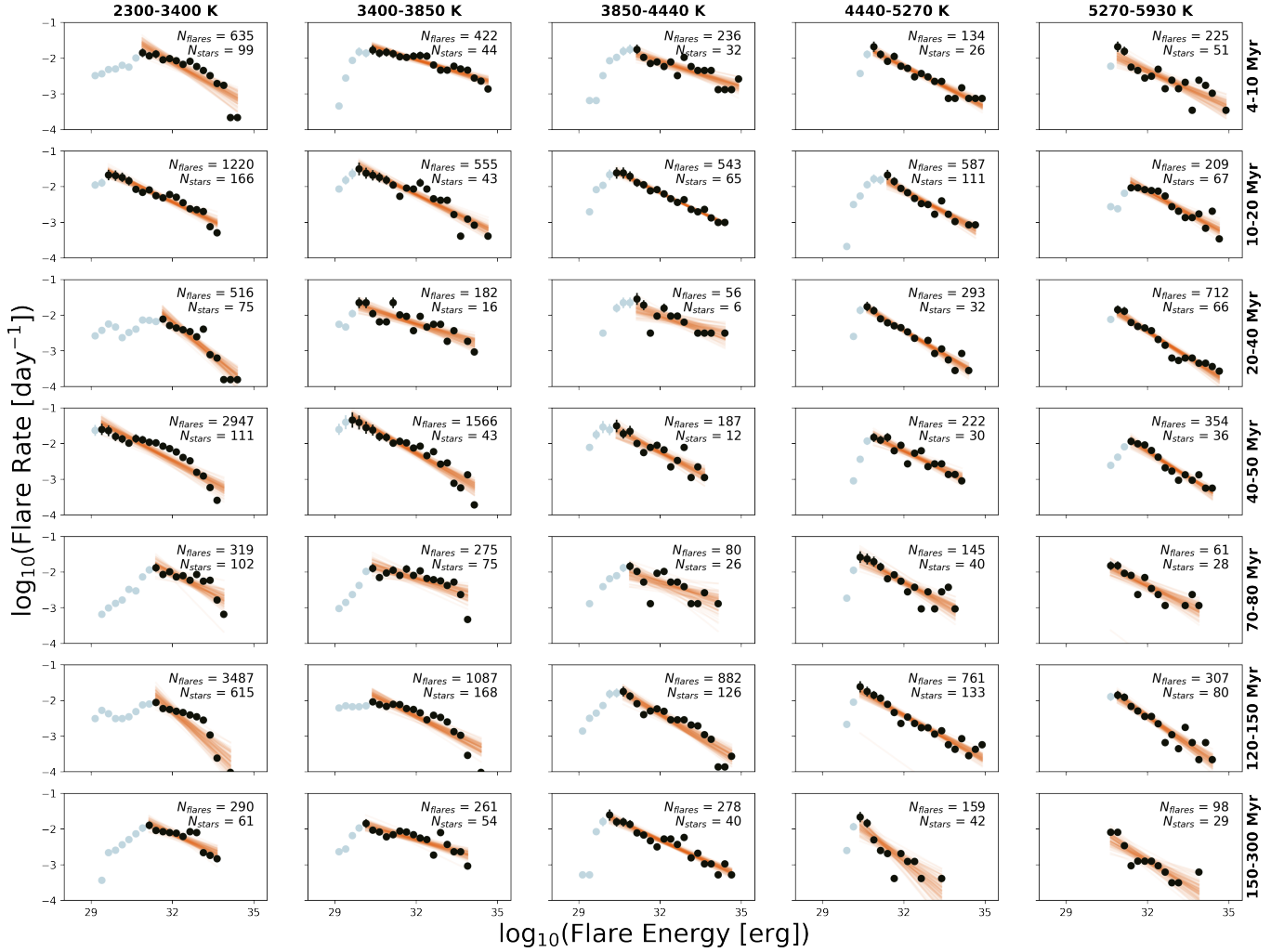


Figure A1. Flare frequency distributions (FFDs) for subgroups of stars, clustered by age and effective temperature, T_{eff} . Flares were binned into 25 bins in log-space from $10^{27} - 10^{35}$ erg. We fit the FFD from the turn-over in the binned flares, likely a result of very low-energy flares being missed in our flare-detection algorithm. The bins used to fit the FFD are shown in black, while all bins are shown in gray. We ran an MCMC fit to these distributions with a simple power law; 100 random samples from these fits are over-plotted in orange. We fit distributions with > 3 bins. The best-fit slopes from these fits are presented in Figure 3.

Chen, H., Zhan, Z., Youngblood, A., et al. 2021, *Nature Astronomy*, 5, 298, doi: [10.1038/s41550-020-01264-1](https://doi.org/10.1038/s41550-020-01264-1)

Clette, F., Svalgaard, L., Vaquero, J. M., & Cliver, E. W. 2014, *SSRv*, 186, 35, doi: [10.1007/s11214-014-0074-2](https://doi.org/10.1007/s11214-014-0074-2)

Crosby, N. B., Aschwanden, M. J., & Dennis, B. R. 1993, *SoPh*, 143, 275, doi: [10.1007/BF00646488](https://doi.org/10.1007/BF00646488)

Curtis, J. L., Agüeros, M. A., Mamajek, E. E., Wright, J. T., & Cummings, J. D. 2019, *AJ*, 158, 77, doi: [10.3847/1538-3881/ab2899](https://doi.org/10.3847/1538-3881/ab2899)

Davenport, J. R. A. 2016, *ApJ*, 829, 23, doi: [10.3847/0004-637X/829/1/23](https://doi.org/10.3847/0004-637X/829/1/23)

Davenport, J. R. A., Covey, K. R., Clarke, R. W., et al. 2019, *ApJ*, 871, 241, doi: [10.3847/1538-4357/aafb76](https://doi.org/10.3847/1538-4357/aafb76)

Davenport, J. R. A., Mendoza, G. T., & Hawley, S. L. 2020, *AJ*, 160, 36, doi: [10.3847/1538-3881/ab9536](https://doi.org/10.3847/1538-3881/ab9536)

Davenport, J. R. A., Hawley, S. L., Hebb, L., et al. 2014, *ApJ*, 797, 122, doi: [10.1088/0004-637X/797/2/122](https://doi.org/10.1088/0004-637X/797/2/122)

Feinstein, A. D., Montet, B. T., Ansdell, M., et al. 2020, *AJ*, 160, 219, doi: [10.3847/1538-3881/abac0a](https://doi.org/10.3847/1538-3881/abac0a)

Feinstein, A. D., Seligman, D. Z., Günther, M. N., & Adams, F. C. 2022, *ApJL*, 925, L9, doi: [10.3847/2041-8213/ac4b5e](https://doi.org/10.3847/2041-8213/ac4b5e)

Feinstein, A. D., Montet, B. T., Foreman-Mackey, D., et al. 2019, *PASP*, 131, 094502, doi: [10.1088/1538-3873/ab291c](https://doi.org/10.1088/1538-3873/ab291c)

Foreman-Mackey, D., Hogg, D. W., Lang, D., & Goodman, J. 2013, *PASP*, 125, 306, doi: [10.1086/670067](https://doi.org/10.1086/670067)

- Gagné, J., Fontaine, G., Simon, A., & Faherty, J. K. 2018a, *ApJL*, 861, L13, doi: [10.3847/2041-8213/aacdff](https://doi.org/10.3847/2041-8213/aacdff)
- Gagné, J., Mamajek, E. E., Malo, L., et al. 2018b, *ApJ*, 856, 23, doi: [10.3847/1538-4357/aaae09](https://doi.org/10.3847/1538-4357/aaae09)
- Gaia Collaboration, Prusti, T., de Bruijne, J. H. J., et al. 2016, *A&A*, 595, A1, doi: [10.1051/0004-6361/201629272](https://doi.org/10.1051/0004-6361/201629272)
- Gaia Collaboration, Brown, A. G. A., Vallenari, A., et al. 2018, *A&A*, 616, A1, doi: [10.1051/0004-6361/201833051](https://doi.org/10.1051/0004-6361/201833051)
- Galindo-Guil, F. J., Barrado, D., Bouy, H., et al. 2022, *A&A*, 664, A70, doi: [10.1051/0004-6361/202141114](https://doi.org/10.1051/0004-6361/202141114)
- Goodman, J., & Weare, J. 2010, *Communications in Applied Mathematics and Computational Science*, 5, 65, doi: [10.2140/camcos.2010.5.65](https://doi.org/10.2140/camcos.2010.5.65)
- Günther, M. N., Zhan, Z., Seager, S., et al. 2020, *AJ*, 159, 60, doi: [10.3847/1538-3881/ab5d3a](https://doi.org/10.3847/1538-3881/ab5d3a)
- Hawley, S. L., Davenport, J. R. A., Kowalski, A. F., et al. 2014, *ApJ*, 797, 121, doi: [10.1088/0004-637X/797/2/121](https://doi.org/10.1088/0004-637X/797/2/121)
- Howard, W. S., & MacGregor, M. A. 2022, *ApJ*, 926, 204, doi: [10.3847/1538-4357/ac426e](https://doi.org/10.3847/1538-4357/ac426e)
- İşık, E., van Saders, J. L., Reiners, A., & Metcalfe, T. S. 2023, *SSRv*, 219, 70, doi: [10.1007/s11214-023-01016-3](https://doi.org/10.1007/s11214-023-01016-3)
- Ilin, E., Schmidt, S. J., Davenport, J. R. A., & Strassmeier, K. G. 2019, *A&A*, 622, A133, doi: [10.1051/0004-6361/201834400](https://doi.org/10.1051/0004-6361/201834400)
- Ilin, E., Schmidt, S. J., Poppenhäger, K., et al. 2021, *A&A*, 645, A42, doi: [10.1051/0004-6361/202039198](https://doi.org/10.1051/0004-6361/202039198)
- Jackman, J. A. G., Wheatley, P. J., Acton, J. S., et al. 2021, *MNRAS*, 504, 3246, doi: [10.1093/mnras/stab979](https://doi.org/10.1093/mnras/stab979)
- Jeffers, S. V., Kiefer, R., & Metcalfe, T. S. 2023, *SSRv*, 219, 54, doi: [10.1007/s11214-023-01000-x](https://doi.org/10.1007/s11214-023-01000-x)
- Jenkins, J. M., Twicken, J. D., McCauliff, S., et al. 2016, in *Society of Photo-Optical Instrumentation Engineers (SPIE) Conference Series*, Vol. 9913, Software and Cyberinfrastructure for Astronomy IV, 99133E, doi: [10.1117/12.2233418](https://doi.org/10.1117/12.2233418)
- Kerr, R. M. P., Rizzuto, A. C., Kraus, A. L., & Offner, S. S. R. 2021, *ApJ*, 917, 23, doi: [10.3847/1538-4357/ac0251](https://doi.org/10.3847/1538-4357/ac0251)
- Kilcik, A., Yurchyshyn, V. B., Oztug, A., & Rozelet, J. P. 2014, *ApJL*, 794, L2, doi: [10.1088/2041-8205/794/1/L2](https://doi.org/10.1088/2041-8205/794/1/L2)
- Kounkel, M., Covey, K., & Stassun, K. G. 2020, *AJ*, 160, 279, doi: [10.3847/1538-3881/abc0e6](https://doi.org/10.3847/1538-3881/abc0e6)
- Kretschmar, M. 2011, *A&A*, 530, A84, doi: [10.1051/0004-6361/201015930](https://doi.org/10.1051/0004-6361/201015930)
- Lean, J. 1987, *J. Geophys. Res.*, 92, 839, doi: [10.1029/JD092iD01p00839](https://doi.org/10.1029/JD092iD01p00839)
- Lehtinen, J., Jetsu, L., Hackman, T., Kajatkari, P., & Henry, G. W. 2016, *A&A*, 588, A38, doi: [10.1051/0004-6361/201527420](https://doi.org/10.1051/0004-6361/201527420)
- Lin, J., Wang, F., Deng, L., et al. 2023, *ApJ*, 958, 1, doi: [10.3847/1538-4357/ad0469](https://doi.org/10.3847/1538-4357/ad0469)
- Luger, R., Bedell, M., Foreman-Mackey, D., et al. 2021, *arXiv e-prints*, arXiv:2110.06271, <https://arxiv.org/abs/2110.06271>
- Luhman, K. L. 2007, *ApJS*, 173, 104, doi: [10.1086/520114](https://doi.org/10.1086/520114)
- Maehara, H., Shibayama, T., Notsu, Y., et al. 2015, *Earth, Planets and Space*, 67, 59, doi: [10.1186/s40623-015-0217-z](https://doi.org/10.1186/s40623-015-0217-z)
- Martin, D. C., Fanson, J., Schiminovich, D., et al. 2005, *ApJL*, 619, L1, doi: [10.1086/426387](https://doi.org/10.1086/426387)
- Medina, A. A., Winters, J. G., Irwin, J. M., & Charbonneau, D. 2020, *ApJ*, 905, 107, doi: [10.3847/1538-4357/abc686](https://doi.org/10.3847/1538-4357/abc686)
- Morrissey, P., Conrow, T., Barlow, T. A., et al. 2007, *ApJS*, 173, 682, doi: [10.1086/520512](https://doi.org/10.1086/520512)
- Murphy, S. J., & Lawson, W. A. 2015, *MNRAS*, 447, 1267, doi: [10.1093/mnras/stu2450](https://doi.org/10.1093/mnras/stu2450)
- Notsu, Y., Shibayama, T., Maehara, H., et al. 2013, *ApJ*, 771, 127, doi: [10.1088/0004-637X/771/2/127](https://doi.org/10.1088/0004-637X/771/2/127)
- Okamoto, S., Notsu, Y., Maehara, H., et al. 2021, *ApJ*, 906, 72, doi: [10.3847/1538-4357/abc8f5](https://doi.org/10.3847/1538-4357/abc8f5)
- Oláh, K., Kővári, Z., Petrovay, K., et al. 2016, *A&A*, 590, A133, doi: [10.1051/0004-6361/201628479](https://doi.org/10.1051/0004-6361/201628479)
- Paudel, R. R., Gizis, J. E., Mullan, D. J., et al. 2018, *ApJ*, 858, 55, doi: [10.3847/1538-4357/aab8fe](https://doi.org/10.3847/1538-4357/aab8fe)
- Pecaut, M. J., & Mamajek, E. E. 2016, *MNRAS*, 461, 794, doi: [10.1093/mnras/stw1300](https://doi.org/10.1093/mnras/stw1300)
- Pizzolato, N., Maggio, A., Micela, G., Sciortino, S., & Ventura, P. 2003, *A&A*, 397, 147, doi: [10.1051/0004-6361:20021560](https://doi.org/10.1051/0004-6361:20021560)
- Ricker, G. R., Winn, J. N., Vanderspek, R., et al. 2015, *Journal of Astronomical Telescopes, Instruments, and Systems*, 1, 014003, doi: [10.1117/1.JATIS.1.1.014003](https://doi.org/10.1117/1.JATIS.1.1.014003)
- Röser, S., Schilbach, E., & Goldman, B. 2016, *A&A*, 595, A22, doi: [10.1051/0004-6361/201629158](https://doi.org/10.1051/0004-6361/201629158)
- Saar, S. H., & Brandenburg, A. 1999, *ApJ*, 524, 295, doi: [10.1086/307794](https://doi.org/10.1086/307794)
- Schmitt, J. H. M. M., Ioannidis, P., Robrade, J., Czesla, S., & Schneider, P. C. 2019, *A&A*, 628, A79, doi: [10.1051/0004-6361/201935374](https://doi.org/10.1051/0004-6361/201935374)
- Schneider, A. C., & Shkolnik, E. L. 2018, *AJ*, 155, 122, doi: [10.3847/1538-3881/aaa24](https://doi.org/10.3847/1538-3881/aaa24)
- Seligman, D. Z., Rogers, L. A., Feinstein, A. D., et al. 2022, *ApJ*, 929, 54, doi: [10.3847/1538-4357/ac5b69](https://doi.org/10.3847/1538-4357/ac5b69)
- Shibayama, T., Maehara, H., Notsu, S., et al. 2013, *ApJS*, 209, 5, doi: [10.1088/0067-0049/209/1/5](https://doi.org/10.1088/0067-0049/209/1/5)
- Silverberg, S. M., Kowalski, A. F., Davenport, J. R. A., et al. 2016, *ApJ*, 829, 129, doi: [10.3847/0004-637X/829/2/129](https://doi.org/10.3847/0004-637X/829/2/129)
- Tarricq, Y., Soubiran, C., Casamiquela, L., et al. 2021, *A&A*, 647, A19, doi: [10.1051/0004-6361/202039388](https://doi.org/10.1051/0004-6361/202039388)

- Tofflemire, B. M., Rizzuto, A. C., Newton, E. R., et al. 2021, AJ, 161, 171, doi: [10.3847/1538-3881/abdf53](https://doi.org/10.3847/1538-3881/abdf53)
- Tovar Mendoza, G., Davenport, J. R. A., Agol, E., Jackman, J. A. G., & Hawley, S. L. 2022, AJ, 164, 17, doi: [10.3847/1538-3881/ac6fe6](https://doi.org/10.3847/1538-3881/ac6fe6)
- Webb, D. F., & Howard, R. A. 1994, J. Geophys. Res., 99, 4201, doi: [10.1029/93JA02742](https://doi.org/10.1029/93JA02742)
- Wright, N. J., Drake, J. J., Mamajek, E. E., & Henry, G. W. 2011, ApJ, 743, 48, doi: [10.1088/0004-637X/743/1/48](https://doi.org/10.1088/0004-637X/743/1/48)
- Wright, N. J., Newton, E. R., Williams, P. K. G., Drake, J. J., & Yadav, R. K. 2018, MNRAS, 479, 2351, doi: [10.1093/mnras/sty1670](https://doi.org/10.1093/mnras/sty1670)